Phase-resolved measurement of atmospheric-pressure radio-frequency pulsed discharges in $Ar/CH_4/CO_2$ mixture

Zehui Liu [1, 2], Bangdou Huang [1 *], Wenchao Zhu [4], Cheng Zhang [1, 2 *], Xin Tu [5], and Tao Shao [1, 2, 3]

[1] Institute of Electrical Engineering, Chinese Academy of Sciences, Beijing, 100190, People's Republic of China

[2] University of Chinese Academy of Sciences, Beijing, 100049, People's Republic of China

[3] Dalian National Laboratory for Clean Energy, Dalian, 116023, People's Republic of China

[4] State Key Laboratory of NBC Protection for Civilian, Beijing, 102205, People's Republic of China

[5] Department of Electrical Engineering and Electronics, University of Liverpool, Liverpool, L69 3GJ, United Kingdom

[*]Author to whom any correspondence should be addressed.
E-mail: zhangcheng@mail.iee.ac.cn, and huangbangdou@mail.iee.ac.cn

Abstract

In order to comprehensively investigate the discharge characteristics of an atmospheric-pressure radio-frequency (RF) pulsed discharge in $Ar/CH_4/CO_2$, a phase-resolved measurement is given in this paper. Firstly, the discharge characteristics of RF plasma in a gas mixture of Ar, CO_2 and CH_4 are investigated under different parameters. It is found peak power is more efficient than duty cycle in increasing the discharge area. Besides, a phase-resolved morphology of RF plasma is given. The discharge in the positive cycle is longer in length and stronger in emission intensity than in the negative cycle. Secondly, different activation paths of species have been obtained by using phase-resolved optical emission spectroscopy. Ar species is mainly activated by electron collision effect, while CH and C_2 are mainly activated by Ar metastable species. Finally, detailed electron kinetics is analyzed. The results show that most energy is transferred to the vibrational excitation compared to elastic activation, electronic excitation, and ionization under different ratios of CO_2 and CH_4 to Ar. Besides, under a higher ratio of CH_4 and CO_2 to Ar, the generating rate of species and power loss rate are higher. It proves that higher fraction of CO_2 and CH_4 is better for the conversion rate and energy efficiency under RF discharge in theory, which guides the reforming of CH_4 and CO_2 in RF discharge.

Keywords: radio-frequency plasma, optical emission spectroscopy, dry reforming of methane, discharge characteristics, activation modes

1. Introduction

Dry reforming of methane (DRM), a reaction that converts methane and carbon dioxide to synthesis gas (H_2 and CO), offers a promising method of global carbon balance management [1-3]. Generally, high temperature is necessary to activate CH_4 and CO_2 during traditional DRM process. It brings the problem of low energy efficiency and catalyst deactivation caused by carbon deposition in conventional thermal and catalytic technology [4]. Non-thermal plasma (NTP) is an eco-friendly technology that can produce high-energy electrons and reactive species at low temperatures and it has been used in DRM [5]. Among different kinds of NTP discharge form, including corona discharge [6, 7], dielectric barrier discharge (DBD) [8, 9], spark discharge [10,

11], gliding arc discharge [12, 13], radio-frequency (RF) discharge [14, 15], etc., RF discharge is of great importance for the superiority in its low reduced electric field, high electron density and high power density over low-frequency discharge [16, 17].

RF discharge was used for DRM in 1976 by Capezzuto *et al.* [18] under 20 Torr, and they found the formation of CO was via the intermediate C_2-hydrocarbons. Savinov *et al.* [14] investigated the decomposition of methane and carbon dioxide over a range of pressures of 5-60 Torr by using capacitive RF discharge. They found that the conversion of each gas depended on the specific energy of the molecules, and the major gaseous products were C_2, C_3 and CO. However, a low-pressure condition requires a more complicated and expensive piece of equipment. Yao *et al.* [19] studied the oxidative coupling and reforming of CH_4 and CO_2 by using a repetitive pulsed plasma, and the results indicated that the energy efficiency and conversion rate were improved by increasing pulsed frequency. However, this experiment is assisted by a temperature as high as 500 ºC. Indeed, at ambient temperature and pressure, it is difficult to discharge with pure CH_4 and CO_2 under RF source. Okumoto *et al.* [20] found that increasing the inert gas concentration generated a much more intense discharge and consequently enhanced the conversion of methane. Therefore, an atmospheric-pressure radio-frequency (RF) pulsed discharge in $Ar/CH_4/CO_2$ is investigated in this paper.

Furthermore, optical emission spectroscopy (OES) is an in-situ and non-intrusive method of gaining insight into the characteristics of the plasma [21, 22], so OES diagnostics have been widely used to investigate RF discharge. Luo *et al.* [21] performed an in-situ OES analysis of the activities of CH and H species in a CH_4/He RF discharge plasma and found that the luminous intensity of CH and H species increased first and then decreased with the increase of power. Yuan *et al.* [22] measured the OES of an Ar/C_2H_5OH discharge at 33 MHz and reported that the luminous intensity of C, CN, CH and C_2 carbonaceous species were strengthened with the increase of C_2H_5OH, while that of Ar was decreased as the addition of ethanol decreased the electron temperature. However, OES studies of DRM in RF discharges are still lacking. This is especially true of discharges at atmospheric pressure, which is necessary for the practical application of DRM.

In this paper, the discharge characteristics of the CH_4/CO_2/Ar RF discharge under different gas flow rates, gas ratios, and powers were investigated. Especially, a phase-resolved OES of typical emissive species has been measured within an RF cycle, based on which, the generation paths of different species were analyzed. Not only the changes in luminous intensity of the species were obtained, but also key parameters such as the gas temperature and the generation rate of typical species were calculated and compared under different gas ratios. Finally, the reduced electric field (E/N) was calculated and the corresponding electron kinetics under different gas ratios were analyzed.

2. Experimental Setup

Fig. 1a shows a schematic diagram of the experimental system. The plasma is generated by a 13.56 MHz power source, accompanying with an automatic matching network (Beijing GM power technology). The source can work in a pulsed mode, which varies from 1 Hz to 10 kHz, and the duty cycle can be varied from 1% to 99%. The maximum output power is 500 W. The discharge reactor has a coaxial cylindrical geometry, as shown in Fig. 1b. The plasma is generated inside a quartz tube with an inner diameter of 1.6 mm and an outer diameter of 3 mm. A hollow stainless-steel tube, with an outer diameter of 1.5 mm, is inserted into the quartz tube and performs as the high-voltage (HV) electrode. A 10 mm width copper foil is wrapped outside of the quartz tube as the ground electrode, namely the length of the ground electrode is 10 mm. The tip of the HV electrode is placed at the middle (i.e. 5-mm position) of the ground electrode. One side of the quartz tube is open to air, and it is ~ 2.5 cm away from the tip of the HV electrode.

The voltage on the HV electrode is measured by a high-voltage probe (Tektronix DPO 2024) while the current waveform is monitored by a current probe (Pearson, model 4100, 1V/A). The waveforms are recorded by a digital oscilloscope (Lecroy WR204Xi) with a bandwidth of 2 GHz and a sample rate of 10 GS/s.

CH_4 (99.999%) and CO_2 (99.999%) are used as reaction gases, and Ar (99.999%) is used as a carrier gas in this experiment. The flow rate of each gas is controlled by a mass flowmeter (Sevenstar D07-19). These different gases are firstly mixed by a gas mixer and then flow into the quartz tube through a hollow stainless-steel tube.

Fig. 1c shows a typical voltage waveform on the HV electrode. Before the breakdown happens, the voltage keeps increasing, as the circuit has a high Q-factor without the discharge. The breakdown voltage occurs when the voltage reaches about 150 V. After the discharge is initiated, the voltage starts to decay, as the resistance of the plasma dissipates the RF power and the Q-factor of the circuit drops [23]. After several microseconds, the voltage amplitude maintains at a constant value, which means that the plasma turns into a quasi-stable state. The current wave presents a similar trend with the voltage wave.

Optical emission spectroscopy (OES) is used to analyse the reactive species by using emitted spectral lines. OES has the advantage of in-situ, real-time online and no disturbance, and can be easily used in the analysis and diagnosis of the temporal and spatial distribution of reactive species [24]. It is an effective method of studying the transition of excited state and mechanism of energy transfer [25-27].

In order to perform a phase-resolved measurement, a delay generator (SRS DG645) is used to synchronize the RF discharge with an ICCD (Andor DH334T-18U-03). When measuring the discharge image, a camera lens (Cannon EOS 500D) is mounted directly on an ICCD camera. When measuring the OES, fiber is used to collect the emission light from the discharge, which is delivered to a spectrometer (Andor Shamrock 500i) with an 1800 l/mm grating.

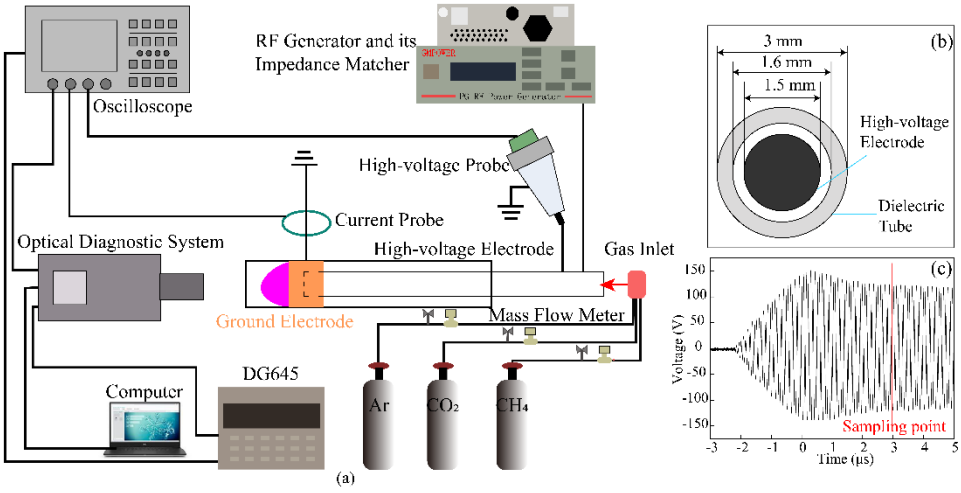

Figure 1. A schematic diagram of the experimental setup (a), the cross section of the reactor (b), and a typical voltage waveform on the HV electrode (c).

3. Results and Discussion

3.1 Imaging of Discharge

3.1.1 Effect of Gas Flow Rate and Gas Ratio

The volume of discharge can influence the conversion rate of DRM by changing the residence time [28]. Therefore, discharge characteristics are studied under different gas flow rates, gas ratios and discharge power. Fig. 2a presents discharge images

with different gas flow rates, i.e. ~ 1 to 3 standard liter per minute (slm) of the mixing gas (0.5% CH_4 + 0.5% CO_2 + 99% Ar). The RF source is operated at 100 Hz with a duty cycle of 30% and a discharge power of 30 W. The single shots are taken by ICCD with an exposure time of 0.1 s and a gain of 100. The white squares marked in Fig. 2 and Fig. 3 are the location of the ground electrode, while the HV electrode is 5 mm away from the left boundary of the ground electrode, which is not in the figure. There is no obvious difference in discharge length when changing the gas flow rate, while under pure Ar RF discharge, the discharge length increases significantly with the increase of the gas flow rate [26], this is because CH_4 and CO_2 are molecular gas, and they are hard to be ionized.

The length of the discharge region is about 4 mm under different gas flow rates. The area of discharge (from the side view) under 2 slm is a little larger than 1 slm discharge. When the gas flow is over 2 slm, the discharge length and discharge area have no obvious increase with the increase of the gas flow. In all the pictures, the light intensity is stronger near the electrode, which indicates a stronger discharge, and the intensity of the discharge away from the electrode is weaker. This is because the electric field near the electrode is strongly distorted.

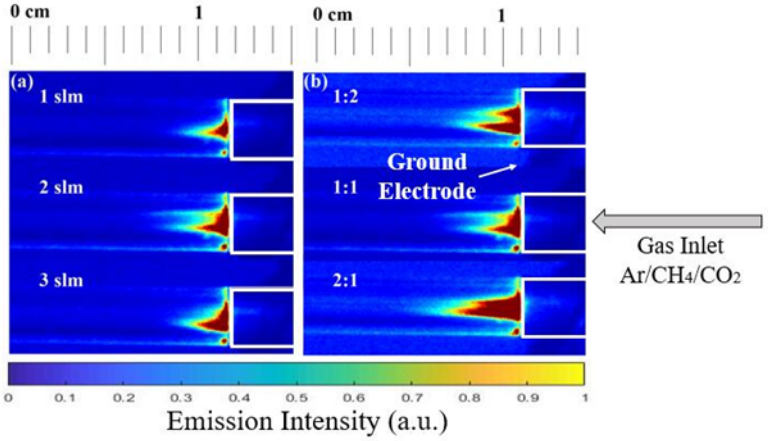

Figure 2. Discharge images with different gas flow rates (a) and with different ratios of CH_4 to CO_2 (b) when the frequency is 100 Hz, the duty cycle is 30% and the discharge power is 30 W. The images are taken by ICCD with an exposure time of 0.1 s and a gain of 100.

Fig. 2b shows discharge images under different gas ratios. In the experiment, the total gas flow rate is fixed at 2 slm. CH_4 and CO_2 accounts for 1% of the total flow, while the ratio of CH_4 to CO_2 is set as 1:2, 1:1 and 2:1, respectively. And the parameters of the RF source is the same with Fig. 2a.

Even though there is a very small difference in the gas component, there is an obvious change in discharge character. When the ratio of CH_4 to CO_2 is less than 1, the discharge has two obvious separated tips, and the length of discharge is shorter. When the concentration of CH_4 is increased, one of the tips is disappearing leaving with a weak light region. When CO_2 is less than CH_4, both the length and area of the discharge region increase, which indicates a stronger discharge. It is known that CO_2 is an electronegative gas, and the increase of CO_2 concentration will decrease the mean electron energy [22], so that when CO_2 increases, the discharge intensity will be decreased [29-31].

3.1.2 Effect of Discharge Power

RF source can work in a pulsed mode, and it has many parameters to modify, which can satisfy different reactions' needs. For example, when using a pulsed mode, the carbon deposition problem caused by overheat may be alleviated. In this work, the effect of peak power and duty cycle on the discharge characteristics are investigated.

Fig. 3 shows discharge images of different power parameters, i.e. peak power and duty cycle. In Fig. 3a, the frequency is 100 Hz, the duty cycle is 30%, and the power is changing from 20 W to 60 W. In Fig. 3b, the frequency is 100 Hz, the peak power is 30 W, and the duty cycle changes from 20% to 60%. The whole gas flow rate is 2 slm, while CH_4 and CO_2 account for 0.5% of the whole gas flow rate, respectively. The images are taken by ICCD with an exposure time of 0.1 s and a gain of 100.

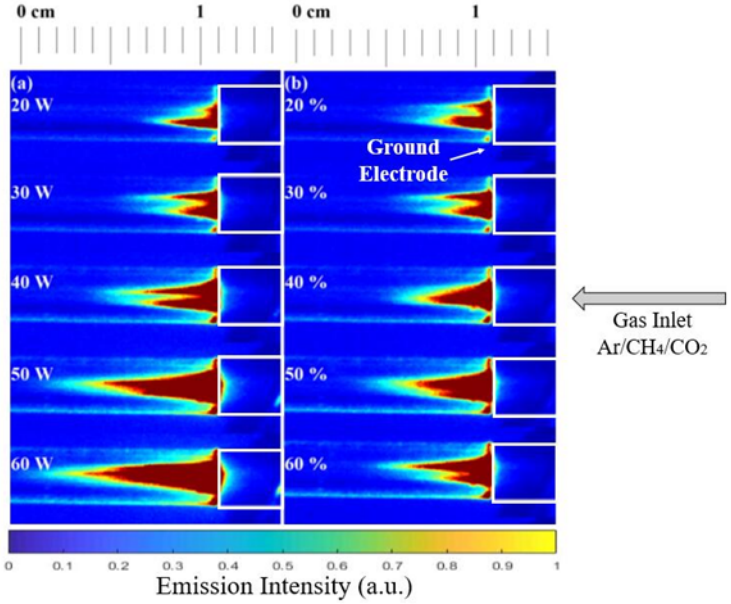

Figure 3. The discharge images with different peak powers (a) and different duty cycles (b) under a condition of whole gas flow rate of 2 slm (0.5% CH_4 + 0.5% CO_2 + 99% Ar). The frequency is 100 Hz. The images are taken by ICCD with an exposure time of 0.1 s and a gain of 100.

Peak power and duty cycle, the two parameters change the coupling energy from different aspects, while peak power is modulating the whole power in a cycle, duty cycle is modulating the working time in a cycle while the peak power keeps invariant. In Fig. 3a, with the increase of peak power, the length of the discharge region increases significantly, while in Fig. 3b, with the increase of duty cycle, the length of the discharge region is increased slightly. Comparing Fig. 3a with Fig. 3b, the mean power in the figures on the same line is the same, especially for figures at the second line, the discharge is under the same experimental condition (i.e. 30 W * 30%). The mean power of the discharge is peak power times the duty cycle, so 40 W times 30% equals to 30 W times 40%. When the peak power is more than 30 W and the duty cycle is more than 30%, even with the same mean power input, discharge is quite different. The discharge operating with a higher peak power is more intensive than that operating with a larger duty cycle. Therefore, the experiment result indicates that higher peak power is more efficient than a longer pulse width in strengthening the discharge. A problem should be noted in Fig. 2 and Fig. 3, the discharge characteristics under the same condition that gas flow rate of 2 slm, peak power of 30 W, duty cycle of 30% seems different. This is caused by the different contrast ratios set in the post-processing by a calculation software.

Figs. 2 and 3 together provide basic information about the discharge characteristics for different parameters. A small change in the gas components can significantly alter the discharge, while the increase of gas flow rate slightly affects the discharge. Increasing the setup power by the peak power or the duty cycle will strengthen the discharge, and the peak power influences the discharge more strongly.

3.2 Phase-resolved Discharge Images

Although discharge images with a long enough integral time of 0.1 s have been obtained, the research confirms that in one RF cycle (≈ 75 ns), the discharge has a development process. During one RF discharge cycle (Fig. 1c), the discharge characteristics are investigated. The discharge initiates after several sinusoidal cycles. The length of discharge area begins to increase after the breakdown occurs and then the length reaches the maximum. The discharge is nearly the same in each sinusoidal cycle after breakdown. When the duty cycle finishes, the voltage amplitude decreases to zero right away so that the discharge process ends quickly without ramping down. So a sampling point (marked in Fig. 1c) during the stable discharge period is chosen to analyze the phase-resolved discharge images.

A representative phase-resolved discharge images have been investigated under a gas flow rate of 1 slm, with 98% Ar + 1% CO_2 + 1% CH_4. The frequency is 100 Hz, the duty cycle is 30%, and the peak power is 20 W. The images are taken by ICCD with a gate width of 5 ns and a gain of 3000. In this way, the evolution of the discharge image during one RF cycle (≈ 75 ns) is obtained. DG645 has been used to synchronize the discharge and ICCD. The ICCD combined with the camera lens has been mounted directly towards the tube (axial view) and outside the ground electrode towards the discharge region (side view).

The white square marked in Fig. 4a represents the ground electrode, dashed line in Fig. 4a and solid line in Fig. 4b tell the location of the quartz tube. We have noticed a distinct difference between the discharge images from the side view and the axial view. From the side view, there is one occurrence of intensity enhancement (during 15 to 45 ns) within one RF cycle. However, from the axial view, two occurrences of intensity enhancement process appear during 15 - 45 ns and 55 - 75 ns. From the axial view, the tube is always luminous throughout the whole cycle. It should be noted that the location of the discharge area is asymmetric to the quartz tube, which is caused by the asymmetric installation of the HV electrode.

The electrons have an oscillating motion that they are decelerated in the wave frame and momentarily move back towards the HV electrode during the sheath expansion [32, 33], which is hidden by the ground electrode, corresponding to 50 – 75 ns, and again, advancing into the sheath region, which corresponds to 5 – 45 ns. The electron heating process in RF plasma is ‘asymmetric’ due to the sheath oscillation within one RF cycle [34, 35]. During the sheath expansion process, the electrons obtain more acceleration near the sheath region. For example, the mean electron energy is higher around the ground electrode in the positive half cycle while the mean electron energy is higher around the HV electrode in the negative half cycle. Besides, the discharge in the positive half cycle has more electron density than negative time domain [36], so it is not enough to sustain the discharge in the region outside the electrode during the negative half cycle [37]. Therefore, two occurrences of intensity enhancement correspond to the regions near the ground electrode and HV electrode, respectively. For the axial view, the tube is always luminous because it shows the discharge that happens throughout the whole cycle.

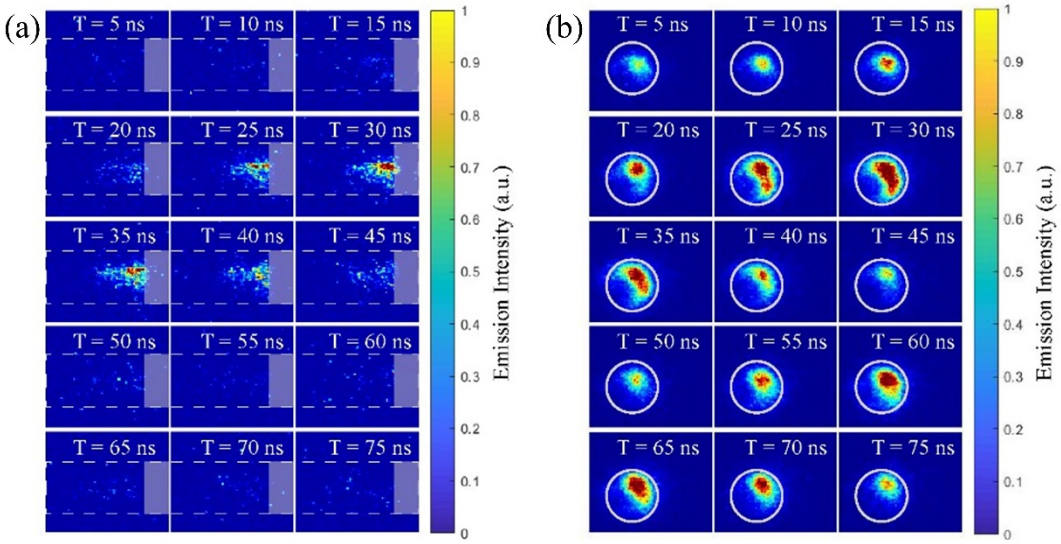

Figure 4. The phase-resolved discharge images from the side view (a) and the axial view (b). The gas flow rate is 1 slm, with 98% Ar + 1% CO_2 + 1% CH_4. The frequency is 100 Hz, the duty cycle is 30%, and the peak power is 30 W. The single shots are taken by ICCD with an exposure time of 5 ns and a gain of 3000.

3.3 Optical Emission Spectroscopy

3.3.1 Typical OES from the discharge

Time-averaged optical emission spectroscopy is taken to identify the species in the RF discharge region, as shown in Fig. 5. The discharge parameters are the same as that of Fig. 4 (frequency of 100 Hz , peak power of 20 W, duty cycle of 30%, gas flow rate of 1 slm and gas concentration of 1% CH_4 + 1% CO_2 + 98% Ar). The OES is taken by ICCD with fiber. The exposure time is 1 s and the gain is 3500.

Species like OH, CH, C_2, O and Ar, etc., are marked in Fig. 5. In RF discharge, CH $A^2\Delta - X^2\Pi$ band is identified at 431.4 nm [38, 39]. C_2 swan band system ($A^3\Pi_g - X'^3\Pi_u$) is identified at 469.7, 471.5, 473.7, 516.5, 558.5 and 563.5 nm [39]. OH $A^2\Pi - X^2\Pi$ band is identified at ~ 307 nm. CO $B^1\Sigma - A^1\Pi$ band appears at 561.0 nm [2]. Optical emission of O atom is identified at 777.3 and 844.7 nm [40]. The appearance of the optical emission from N_2 and CN is due to the interaction between the long lifetime active species (Ar metastable species etc.) in the downstream of the jet discharge with the ambient air.

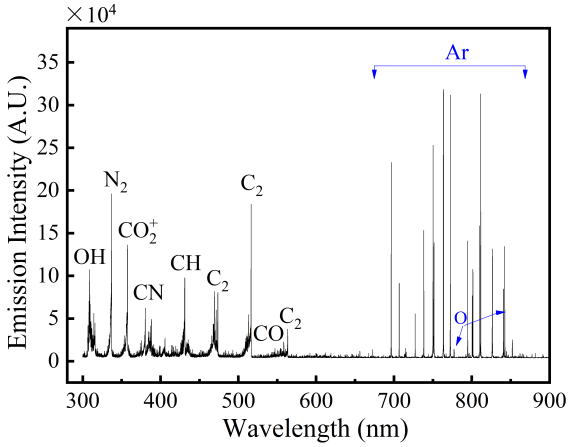

Figure 5. The time-averaged OES from the discharge. The frequency is 100 Hz, the duty cycle is 30%, and the peak power is 20 W. The mixing gas is at a flow rate of 1 slm with 1% CH_4 + 1% CO_2 + 98% Ar. The shot is taken by ICCD with an exposure time of 1 s and a gain of 3500.

3.3.2 Phase-resolved OES

The electrons and excited species have a non-steady state within one RF cycle [41]. This is because the electron energy is affected by the RF electric field [42] and the characteristic time scale of electron energy loss is shorter than the period of an RF cycle [25, 28, 32]. Phase-resolved OES measurement could give characteristics of species in one RF cycle every several nanoseconds, which is necessary for atmospheric RF discharge.

The emission intensity of each species during one phase cycle is investigated to analyze the mechanisms of activation process. And a comparison of 98% Ar + 1% CH_4 + 1% CO_2 (simplified as 2% CH_4 + CO_2) and 99.6% Ar + 0.2% CH_4 + 0.2% CO_2 (simplified as 0.4% CH_4 + CO_2) is performed to analyze the activation modes of different species' activity. The discharge is operated under a frequency of 100 Hz, peak power of 20 W, duty cycle of 30% and a total gas flow rate of 1 slm. The phased-resolved OES are taken by ICCD with a gate width of 5 ns and a gain of 3500.

The species in this reaction can be divided into two kinds. One is Ar, as the feed gas species, which is activated by electron impact excitation. Adding Ar in CH_4 and CO_2 will increase the conversion rate of CH_4 and CO_2 and strengthen the discharge [43-45]. Another is the reaction gas species that CH_4, CO_2 and their intermediate products and decomposition products, and the activation paths of these two species can be activated by both the electron collision effect and the Penning process with the excited Ar species [40].

Two typical spectra of feed gas species and reaction gas species are chosen to analyze the activity of different species in an RF cycle, respectively. They are Ar spectra at 750 nm (Ar1) and 811 nm (Ar2) and two typical spectra of intermediate reaction products of CH_4 and CO_2, which are 431 nm (CH) and 516 nm (C_2), respectively. CH and C_2 are the main intermediate products of CH_4 [46], and in this paper, these two species are used to represent the conversion of CH_4. A reasonable assumption is made here that the conversion of CO_2 is also represented by CH and C_2. This is because CH_4 and CO_2 are molecular gas, they are both hard to be ionized and the final products (H_2 and CO) of CH_4 and CO_2 always show the same changing trends when the discharge frequency, pulse peak width and some other parameters are changed [2]. By modifying the ratio of CH_4 and CO_2 to Ar, we can give an insight into the mechanism of the reaction paths.

The phase-resolved OES of typical species under different ratios of CH_4 and CO_2 is shown in Fig. 6, and a calculated modulation ratio of different species under different ratios of CH_4 and CO_2 is shown in Fig. 7. The modulation ratio is calculated by the difference between the maximum emission intensity (I_{max}) and the minimum emission intensity (I_{min}) divided by the mean value of emission intensity (I_{mean}) in an RF cycle.

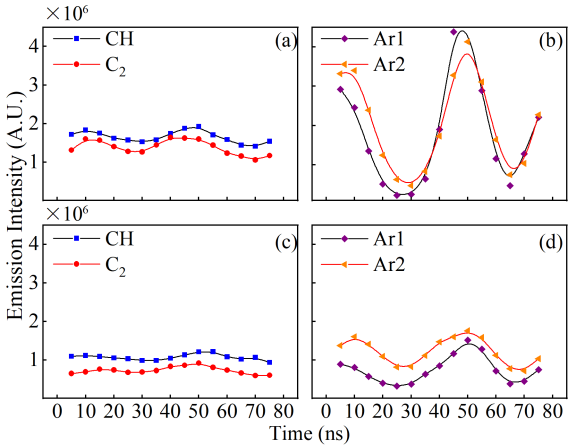

Figure 6. The phase-resolved optical emission intensity of typical species at 2% (a, b) and 0.4% (c, d) of CH_4 and CO_2.

In Fig. 6, the emission intensity of C_2 and CH species increases with the increase of the concentration of CH_4 and CO_2, which indicates a stronger dissociation occurs under a higher concentration of CH_4 and CO_2. As for Ar species, the emission intensity is also increasing with the increase of gas ratio, which is different from [30], this is because the ionization of CH_4 and CO_2 is more difficult than Ar, therefore, a decrease in the Ar concentration means an increase in power density absorbed by Ar species. The emission intensity for the species at the first point and final point in one cycle have no distinct difference. This means that the discharge has reached a quasi-stable state, if its phase-modulation is neglected. Therefore, the variation of duty cycle slightly affects discharge compared to the peak power (Fig. 3).

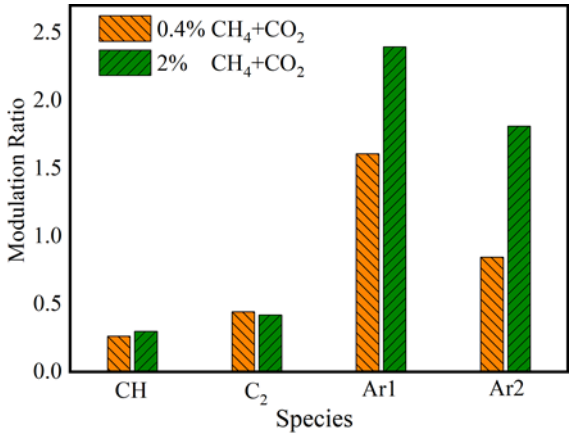

Figure 7. The modulation ratio of typical species at different concentrations.

The temporal evolution of Ar's emission intensity is similar to a sinusoidal wave that fits the voltage waveform, and the modulation ratio of Ar is higher as shown in Fig. 7, indicating that Ar is significantly affected by RF discharge [47], and Ar species are mainly excited by electron impact (path 1). While the modulation ratios of CH and C_2 are lower, CH and C_2 species are slightly affected by RF discharge. Considering the example of CH, the excited species could be generated by 2 paths: the electron impact excitation (path 2) and the Penning process (path 3). The excitation paths are shown below.

$$e + \mathrm{Ar} \rightarrow e + \mathrm{Ar}^* \rightarrow \mathrm{e} + h\upsilon + \mathrm{Ar} \qquad \text{Path 1}$$

$$e + CH_4 \rightarrow e + CH^* + \text{products}$$
$$\rightarrow e + CH + h\nu + \text{products} \qquad \text{Path 2}$$

$$Ar^* + CH_4 \rightarrow Ar + CH^* + \text{products}$$
$$\rightarrow Ar + CH + h\nu + \text{products} \qquad \text{Path 3}$$

Based on Fig. 7, the modulation of the Ar's emission intensity increases with the concentration of $CH_4 + CO_2$, which indicates the electron impact excitation processes (path 1) are sensitive to the addition of molecular gases. The modulation of the emission from CH and C_2 is much smaller than Ar, and not sensitive to the concentration of $CH_4 + CO_2$, which implies that the Penning process (path 3) could contribute a large percent to the generation of these species [47], as the lifetime of Ar metastable species (of the order of 15 – 40 ns) is comparable with an RF cycle [44, 45]. Therefore, generation of Ar metastable species is essential for the conversion of CH_4 and CO_2.

Gas temperature is essential for the analysis of electron kinetics. It can be estimated by simulating the rotational temperature ($T_{rot.}$) of $CH_{A\rightarrow X}$, $CH_{B\rightarrow X}$, , $CH_{C\rightarrow X}$ and $OH_{A\rightarrow X}$ etc. for the energy transfer through rotation-translation excitation was rapid, the rotational temperature ($T_{rot.}$) was considered to be approximately equal to the gas temperature [27, 48]. From Fig. 5, $CH_{A\rightarrow X}$ species have been identified at 431 nm. The phase-resolved OES of $CH_{A\rightarrow X}$ in an RF cycle has been measured. Lifbase software 1.5 [49] is used to simulate $CH_{A\rightarrow X}$ to obtain the gas temperature based on phase-resolved OES, the schematic diagram of gas temperature simulation is shown in Fig. 8.

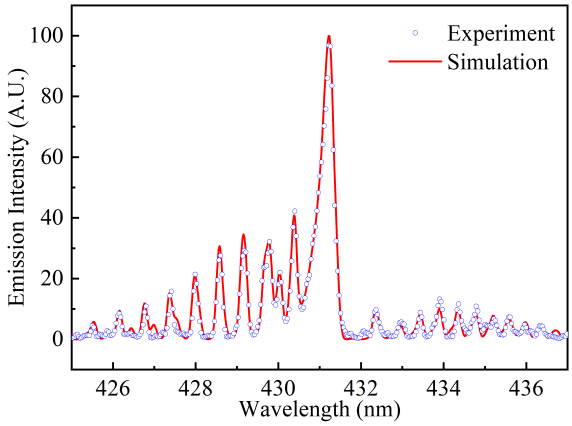

Figure 8. Schematic diagram of gas temperature simulation with Lifbase software.

The gas temperatures throughout a whole RF cycle for both 2% and 0.4% CH_4 and CO_2 discharge are shown in Fig. 9. The mean rotational temperature in 2% CH_4 + CO_2 during a cycle is 950 K±10 K, and the mean vibrational temperature ($T_{vib.}$) is 3800 K±600 K. While in 0.4% CH_4 and CO_2 discharge, the mean rotational temperature in a cycle is 830 K±10 K, and the mean vibrational temperature is 3800 K±600 K. The gas temperature in 2% CH_4 and CO_2 is higher than in 0.4% CH_4 and CO_2. It can be seen that both the rotational temperature ($T_{rot.}$) and the vibrational temperature ($T_{vib.}$) are almost constant during an RF cycle, which verifies that characteristic time for rotational and vibrational relaxation processes of CH species is much longer than an RF cycle.

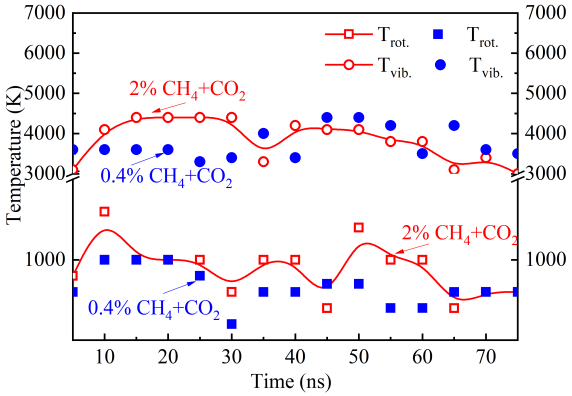

Figure 9. The simulated results of rotational temperature ($T_{rot.}$) and vibrational temperature ($T_{vib.}$) under 0.4% CH_4+CO_2 and 2% CH_4+CO_2, respectively.

When there is more CH and C_2, it means the dissociation of CH_4 and CO_2 is more intensive, therefore it is more likely to form H_2 and CO [46]. So the generating rate of species is calculated.

The simplified time-dependent rate balance equation for the density of excited species n_k can be written as,

$$\frac{dn_k(t)}{dt} = S_k(t) - \frac{n_k(t)}{\tau_k} \quad (1)$$

where $S_k(t)$ is the generation rate of excited k species. τ_k is the lifetime of excited species. In our atmospheric pressure discharge environment, both radiation and collisional quenching processes contribute to the loss of excited species. Therefore, the τ_k can be written as,

$$\frac{1}{\tau_k} = \sum_j A_{k\to j} + \sum_i n_i Q_k^i \quad (2)$$

where $A_{k\to j}$ is the Einstein coefficient of the corresponding radiation process. Q_k^i is the quenching rate coefficient by the i^{th} quencher with its density of n_i (as shown in Table 1).

Table 1 Parameters in the calculation

	750 nm		431 nm	
$A_{k\to j}$	$Ar_{2p1\to 1s2}$	44.7 x10^6	$CH_{A\to X}$	1.8 x10^6
Q_k^i($cm^{-3}s^{-1}$)	$Q_{Ar_{2p1}}^{Ar}$ (300 K)	1.6 x10^{-11}	$Q_{CH_{A\to X}}^{N_2}$ (300 K)	2.3 x10^{-13}
Q_k^i($cm^{-3}s^{-1}$)	$Q_{Ar_{2p1}}^{CH_4}$ (300 K)	9.3 x10^{-10}	$Q_{CH_{A\to X}}^{CH_4}$ (300 K)	2.0 x10^{-11}
Q_k^i($cm^{-3}s^{-1}$)	$Q_{Ar_{2p1}}^{CO_2}$ (300 K)	6.2 x10^{-10}	$Q_{CH_{A\to X}}^{CO_2}$ (300 K)	2.8 x10^{-13}

In an optically thin case, the emission intensity is in proportion to the density of the upper state, i.e. $I_{k\to j} = A_{k\to j} n_k$. Equation 1 can be rewritten as follow:

$$\frac{dn_k(t)}{dt} + \frac{n_k(t)}{\tau_k} = \frac{1}{A_{k\to j}}\left(\frac{dI_{k\to j}(t)}{dt} + \frac{I_{k\to j}(t)}{\tau_k}\right) = S_k(t) \quad (3)$$

The difference between I_{t+5ns} and I_t is divided by Δt to substitute for $\frac{dI_{k\to j}(t)}{dt}$, while the mean value of I_{t+5ns} and I_t substitutes for $I_{k\to j}(t)$ and then $S_k(t)$ of the species are obtained. The calculated $S_k(t)$ is shown in Fig. 10. It can be seen that the RF modulation of $S(t)$ for 750 nm is also larger than that of 431 nm. This result decouples the influence of the lifetime of excited species on the modulation of optical emission intensity. Under a higher gas ratio, the generating rate of CH and C_2 is higher than the lower gas ratio, which implies a higher conversion rate [20, 46]. And the generation of CH and C_2 consumes Ar metastable species, the lag between the generation of CH and C_2 and the generation of Ar species proves the conclusion that

CH is mainly activated by Ar metastable species. Therefore, with a higher gas ratio, it is beneficial for the conversion of CH_4 and CO_2. For DRM, the energy efficiency based on high heating values of the feed gas and products can be calculated as follows:

$$\text{Energy Efficiency} = \frac{\text{LHV of } H_2 \times \text{mole of } H_2 \text{ produced} + \text{LHV of CO} \times \text{mole of CO produced}}{\text{LHV of } CH_4 \times \text{mole of } CH_4 \text{ converted} + P} \quad (4)$$

where P was the discharge power, and LHV is low heating value under 298 K. Under the same discharge condition, when the conversion rate is higher, the energy efficiency is higher [2, 19]. Therefore, with a higher gas ratio, it is beneficial for the energy efficiency as well.

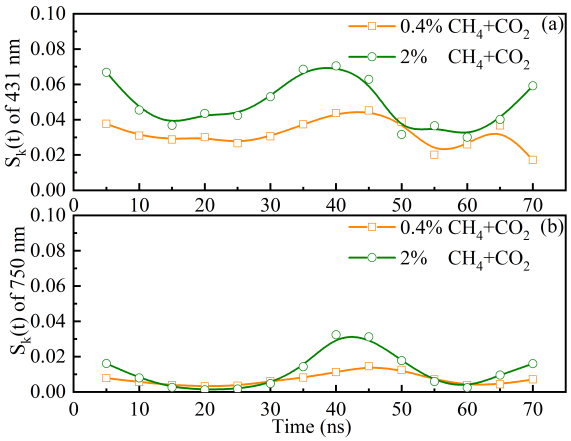

Figure 10. The generating rate $S(t)$ of 431 nm (a), 750 nm (b) under 0.4% CH_4+CO_2 and 2% CH_4+CO_2.

3.4 Analysis of the electron kinetics

The electron energy loss rate and power fraction in Ar/CH_4/CO_2 is analyzed by using BOLSIG+ [50, 51], which is essential to understand the complex chemistry during the discharge, as shown in Figs. 11 and 12. The cross-section data is obtained from the LXCAT database [52]. The electron-electron collisions can be omitted from consideration in the present calculations [53]. All the results are computed under gas temperature of 950 K, which is obtained in the previous study.

Fig. 11 shows the distribution of power loss rate and mean electron energy under different E/N in the discharge. The power loss rate *Power/N* means the energy per unit time absorbed by the electrons from the electric field. In Fig. 11, with the increase of E/N, both *Power/N* and mean electron energy is decreased when there is a higher concentration of CH_4 and CO_2. The energy loss rate in 2% CH_4 + CO_2 is higher than that in 0.4% when E/N is smaller than 100 Td, while the mean electron energy of 2% CH_4 + CO_2 is lower than 0.4% with a range from 1 to 1000 Td.

Mean electron energy in the RF discharge is distributing from 0.06 to 1 eV, which is lower compared to nanosecond discharge [54], but enough to sustain vibrational transition [37]. Vibrational transition is a state-to-state transition, the normal equation is that $e^- + CO_2(0,0,\vartheta_m) \leftrightarrow e^- + CO_2(0,0,\vartheta_n)$ (0.167 eV to 0.5 eV), $e^- + CH_4(0,0,\vartheta_m) \leftrightarrow e^- + CH_4(0,0,\vartheta_n)$ (0.162 eV to 0.361 eV). Vibrational transition makes the inelastic process more efficient and is expected to increase dissociation rates [55, 56]. Therefore, it is beneficial for the activation of CH_4 and CO_2, which is through ladder climbing (stepwise) of vibrational excitation [46] rather than direct dissociation under such low electron energy. After the activation

process, CH_4 and CO_2 are more likely to react with Ar metastable species. And Ar is activated by electron collision, with a higher *Power/N*, more Ar species are activated, and then CH and C_2 are activated by Ar metastable species. This is in favor of the conversion rate and energy efficiency.

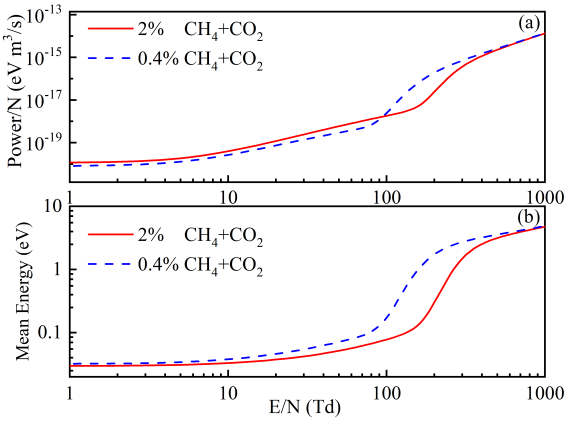

Figure 11. The comparison of power loss rate (a) and mean electron energy (b) in different concentrations of Ar/CH_4/CO_2 analyzed by BOLSIG+.

In Fig. 12, a fractional power loss for different electron-collision processes is shown, and it can be seen that most power is transferred to vibrational excitation process under both 2% and 0.4% CO_2 + CH_4 when *E*/*N* is from 1 to 100 Td. With the increase of *E*/*N*, the energy transferred to the processes of ionization and electronic excitation increases, while energy for elastic process decreases. When *E*/*N* is above 110 Td, most power is transferred to the electronic excitation process, and under a higher ratio of CH_4 and CO_2, the inflection point where energy consumed in electronic excitation process exceeds that consumed in the vibrational excitation process is shifted to higher values of E/N.

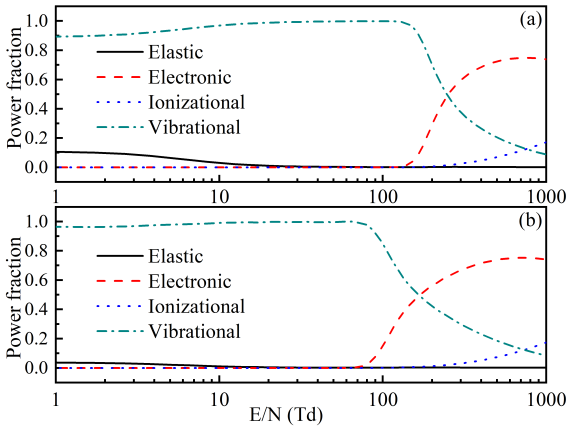

Figure 12. Fractional power losses for each type of process (i.e. elastic activation, electronic excitation, ionizational excitation, vibrational excitation) with 2% CH_4 + CO_2 (a) and 0.4% CH_4 + CO_2 (b).

Under our discharge conditions, an estimation of *E*/*N* should be given. The calculation process is shown as follows:

The equivalent electric field E_H is calculated by [57],

$$E_H^2 = \frac{|\tilde{E}|^2}{2} \frac{\nu_m^2}{\nu_m^2 + \omega^2} \tag{5}$$

$\tilde{E}$ is the conjugate of the actual electric field E. To simplify calculation, E is obtained by an infinite coaxial cylinder geometry, E is estimated as the value of E at the position of the inner border of quartz tube and under the maximum U (i.e. 150 V), ν_m is momentum transfer frequency obtained by BOLSIG+ simulation, ω is the electric field frequency, and the calculation of E_H equals to 4.7 x10^5 V/m.

N is calculated by using the gas temperature obtained in section 3.3.2. When standard gas temperature and gas pressure are substituted in the ideal gas law $pV = \mathrm{NR}T$, N at 950 K is 8.5 x 10^{24}. So E/N is estimated to be about 55 Td.

Although when the ratio of CH_4 and CO_2 to Ar increase from 0.4% to 2%, the power loss rate increases at 55 Td, and the vibrational excitation process accounts for a high percentage of energy consumption, there is need to investigate the electron kinetics when the ratio of CH_4 and CO_2 to Ar continues to increase.

Fig. 13 shows the variation of power fraction and *Power/N* with the increase of gas ratio. The gas temperature is set to 950 K, while *E/N* is set to 55 Td. Elastic and vibrational processes channel most energy under 55 Td because the low electron energy is not enough for electronic excitation and ionization process. The vibrational process channels over 99% of whole energy under different gas ratios, while elastic process consumes little. Though, electron energy decreases with the increase of gas ratio, the power loss rate increases, which indicates a fast energy exchange process happens between the electrons and Ar species. More Ar metastable species are produced and participating in the activation process of CH_4 and CO_2. Therefore, when gas fraction of CH_4 and CO_2 increases, the electron kinetics is better for the conversion. It is testified that lower electron energy implies a higher conversion rate [58]. However, it is hard to ignite the discharge under atmospheric pressure with a high fraction of CH_4 and CO_2 in reality.

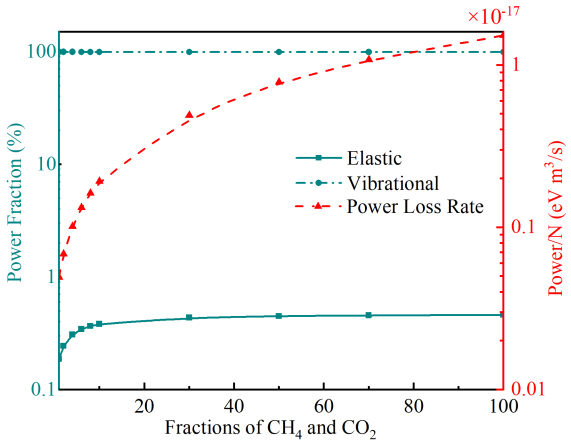

Figure 13. The comparison of power fraction and power loss rate under different fractions of CH_4 and CO_2 (CH_4:CO_2=1) analyzed by BOLSIG+.

4. Conclusion

In this work, the discharge characteristics of an atmospheric pressure RF pulsed discharge have been studied by both experiment and simulation. The discharge morphologies are enhanced by the increase of gas flow rate, ratios of CH_4 to CO_2, and the discharge power. The conversion rate of DRM can be enhanced by appropriately managing the above factors.

In phase-resolved images, because of the oscillating motion of electrons affected by the electric field, discharge characteristics in the positive cycle and the negative cycle are different. Furthermore, different species' modulation ratios in the whole cycle are different. Over the whole cycle of discharge, Ar species is significantly affected by RF electric field,

indicating that Ar species is mainly excited by electron collisions. In contrast, the emission from C_2 and CH was only slightly affected by the RF electric field, which indicates that they are mainly excited by the long-lifetime Ar metastable species.

Based on phase-resolved optical emission spectroscopy, the gas temperature is simulated. The rotational temperature ($T_{rot.}$) and the vibrational temperature ($T_{vib.}$) of $CH_{A\rightarrow X}$ are almost constant during an RF cycle. The mean rotational temperature in 2% CH_4 +CO_2 during a cycle is 950 K±10 K, while in 0.4% CH_4+CO_2 discharge, the mean rotational temperature in a cycle is 830 K±10 K. Additionally, the generating rate of species is calculated. With a higher fraction of CH_4 and CO_2, gas temperature and the generating rate of species are both higher. Besides, the power loss rate *(Power/N*) is higher, indicating that RF discharge under a higher fraction of CH_4 and CO_2 is helpful for the conversion rate and the energy efficiency of DRM.

Acknowledgement

This work was financially supported by National Natural Science Foundation of China (No. 51637010 and No. 51907190), DNL Cooperation Fund, CAS (DNL180204), and the Royal Society – Newton Advanced Fellowship, UK (grant numbers NA140303).

References

1. Markewitz P, Kuckshinrichs W, Leitner W, Linssen J, Zapp P, Bongartz R, Schreiber A, Müller TE (2012) Energy Environ Sci 5:7281-7305
2. Wang XL, Gao Y, Zhang S, Sun H, Li J and Shao T (2019) Appl Energy 243:132-144
3. Tu X, Gallon HJ, Twigg MV, Gorry PA, Whitehead JC (2011) J Phys D Appl Phys 44:274007
4. Nielsen JR, Dibkjaer I, Christiansen LJ (1992) Chemical reactor technology for environmentally safe reactors and products, NATO ASI, NATO
5. Shao T, Wang RX, Zhang C, and Yan P (2018) High Volt 3:14
6. Aziznia A, Bozorgzadeh HR, Seyed-Matin N, Baghalha M, Mohamadalizadeh A (2012) J Nat Gas Chem 21:466-475
7. Yao SL, Okumoto M, Nakayama A, Suzuki E (2001) Energy Fuels 15:1295-1299
8. Okkan A, Dufour T, Arnoult G, De Keyzer P, Bogaerts A, Reniers F (2015) J CO_2 Util 9:78-81
9. Zhang X, Cha MS (2013) J Phys D Appl Phys 46:415205
10. Zhu B, Li X, Liu J, Zhu A (2012) Int J Hydrogen Energy 37:16916-16924
11. Scapinello M, Martini LM, Dilecce G, Tosi P (2016) J Phys D Appl Phys 49:75602
12. Zhu F, Zhang H, Han X, Yan J, Ni M, Li X, Tu X (2017) Fuel 199:430-437
13. Xia Y, Lu N, Wang B, Li J, Shang K, Jiang N, Wu Y (2017) Int J Hydrogen Energy 42:22776-22785
14. Savinov SY, Lee H, Song HK, Na B-K (1999) Ind Eng Chem Res 38:2540-2547
15. Zhang K, Zhang S, Gao Y, Sun H, Yan P, Shao T (2019) Proc Chin Soc Elect Eng 39:3280-3289
16. Park J, Henins I, Herrmann HW, Selwyn GS (2001) J Appl Phys 89:15-19
17. Yang XW, Moravej M, Nowling GR, Chang JP, Hicks RF (2005) IEEE Trans Plasma Sci 33:294-295
18. Capezzuto P, Cramarossa F, d'Agostino R, Molinari E (1977). Revue de Physique Appliquée 12:1205-1208
19. Yao SL, Ouyang F, Nakayama A, Suzuki E, Okumoto M and Mizuno A (2000) Energy Fuels 14:910-914
20. Okumoto M, Kim HH, Takashima K, Katsura S, Mizuno A (2001) IEEE Trans Ind Appl 37:1618-1624
21. Luo LX, Wu WD, Sun WG, Tang YJ, Zhu YH (2007) Chin J Vac Sci Technol 27:203-207
22. Yuan QH, Ren P, Zhou YJ, Yin GQ, Dong CZ (2019) Plasma Sci Technol 21:025402
23. Iza F, Lee JK, Kong MG (2007) Phys Rev Lett 99:075004
24. Levaton J, Klein AN, Binder C (2018) Plasma Chem Plasma Process 38:1259-1272
25. Park J, Henins I, Herrmann HW, Selwyn GS, Hicks RF (2001) J Appl Phys 89:20-28
26. Kraus M, Egli W, Haffner K, Eliasson B, Kogelschatz U, Wokaun A (2002) Phys Chem Chem Phys 4:668-675

27. Wu AJ, Yan JH, Zhang H, Zhang M, Du CM, Li XD (2014) Int J Hydrogen Energy 39:17656-17670
28. Wang Q, Yan BH, Jin Y, Cheng Y (2009) Plasma Chem Plasma Process 29:217-228
29. Li SZ, Wu Q, Wang DZ, Uhm HS (2011) Phys Lett A 375:598-600
30. Moravej M, Yang X, Hicks RF (2006) J Appl Phys 99:093305
31. Pinhão NR, Janeco A, Branco JB (2011) Plasma Chem Plasma Process 31:427-439
32. O'Connell D, Gans T, Vender D, Czarnetzki U, Boswell R (2007) Phys Plasmas 14:034505
33. Vender D, Boswell RW (1992) J Vac Sci Technol A 10:1331-1338
34. Wu SQ, Liu XY, Mao WH, Chen W, Liu C, Zhang CH (2018) J Appl Phys 124:243302
35. Sigeneger F, Schäfer J, Foest R, Loffhagen D (2019) Plasma Sources Sci Technol 28:055004
36. Schulze J, Ganz T, O'Connell D, Czarnetzki U, Ellingboe AR, Turner MM (2007) J Phys D Appl Phys 40:7008-7018
37. Gibson AR, Donkó Z, Alelyani L, Bischoff L, Hübner G, Bredin J, Doyle S, Korolov I, Niemi K, Mussenbrock T (2019) Plasma Sources Sci Technol 28:01LT01
38. Bleekrode R, Nieuwpoort WC (1965) J Chem Phys 43:3680-3687
39. Parigger C, Plemmons DH, Hornkohl JO, Lewis JWL (1994) J Quant Spectroscopy Radiat Transf 52:707-711
40. Kim DB, Jung H, Gweon B, Moon SY, Rhee JK, Choe W (2011) Phys Plasmas 18:043503
41. Garofano V, Montpetit F, Glad X, Gangwar R K, Stafford L (2019) J Vac Sci Technol A 37:021301
42. Crintea DL, Luggenhölscher D, Kadetov VA, Isenberg Ch, Czarnetzki U (2008) J Phys D Appl Phys 41:082003
43. Floettmann K (2015) Phys Rev Accel Beams 18:064801
44. Kolts JH, Setser DW (1978) J Chem Phys 68:4848-4859
45. Velazco JE, Kolts JH, Setser DW (1978) J Chem Phys 69:4357-4373
46. Bogaerts A, Berthelot A, Heijkers S, Kolev St, Snoeckx R, Sun S, Trenchev G, Laer KV, Wang W (2017) Plasma Sources Sci Technol 26:063001
47. Nguyen T, Hernandez E, Donnelly VM, Economou DJ (2018) J Vac Sci Technol A 36:04F406
48. Stanfield SA, Menart J (2009) AIAA J 47:1107-1115
49. Luque J, Crosley DR (1999) Lifbase, database, spectral simulation for OH A-X, OD A-X, NO A-X, B-X D-X CH A-X, B-X, C-X CN B-X, SiH A-X, CF A-X (Version 1.5), SRI International, US
50. Hagelaar GJM, Pitchford LC (2005) Plasma Sources Sci Technol 14:722-733
51. Yamabe, Buckman, Phelps (1983) Phys Rev 27:1345-1352
52. PHELPS database (2013) http://www.lxcat.net. Accessed June 4, 2018
53. Janeco A, Pinhão NR, Guerra V (2015) J Phys Chem C 119:109-120
54. Shao T, Long KH, Zhang C, Yan P, Zhang SC, Pan RZ (2008) J Phys D Appl Phys 46:215203
55. Cascella M, Curik R, Gianturco FA (2001) J Phys B-At Mol Opt 34:705-723
56. Pietanza LD, Colonna G, D'Ammando G, Laricchiuta A, Capetelli M (2016) Chem Phys 468: 44-52
57. Lieberman MA, Lichtenberg AJ. Principles of plasma discharges and materials processing (2015). John Wiley & Sons
58. Zhang DY, Huang Q, Devid EJ, Schuler E, Shiju NR, Rothenberg G, Rooij GV, Yang RL, Liu KZ, Kleyn AW (2018) J Phys Chem C 122:19338-19347